IEEE Access
Multidisciplinary | Rapid Review | Open Access Journal

Date of publication xxxx 00, 0000, date of current version xxxx 00, 0000.

Digital Object Identifier 10.1109/ACCESS.2017.DOI

Analysis and Implementation of LiFi Dimming Systems

TRANG NGUYEN, MOHAMED SUFYAN ISLIM, AND HARALD HAAS
LiFi Research and Development Centre, School of Engineering, The University of Edinburgh, Edinburgh, EH9 3JL, UK

Corresponding author: Harald Haas (e-mail: h.haas@ed.ac.uk).

Harald Haas acknowledges the financial support from the Wolfson Foundation and the Royal Society. All authors acknowledge the financial support from the Engineering and Physical Sciences Research Council (EPSRC) under Established Career Fellowship grant EP/R007101/1.

ABSTRACT The integration of dimming and communication is required in light fidelity (LiFi) systems. The implementation of a visible light communication system with a high signal to noise ratio (SNR) and a wide dimming support range is demonstrated in this paper. Two orthogonal frequency division multiplexing (OFDM) techniques are considered due to the popularity of multi-carrier modulation schemes in enabling high speed LiFi systems. These techniques are: direct current (DC)-biased optical OFDM (DCO-OFDM) and augmented spectral efficiency discrete multi-tone (ASE-DMT). Different dimming methods are proposed: amplitude-modulation (AM) dimming and pulse-width-modulation (PWM) dimming. The proposed system is implemented on a National Instruments (NI) PXIe-1085 and NI-7966R Field Programmable Gate Array (FPGA). The theoretical analysis and simulation results are also presented. ASE-DMT is experimentally shown to provide a nearly constant SNR of up to 26 dB within its entire PWM dimming range from 16% to 84% brightness. DCO-OFDM performance peaks at 30 dB when the dimming level is at 50% and monotonically decreases at other higher and lower dimming levels. ASE-DMT outperforms DCO-OFDM for all dimming levels lower than 30% or higher than 70%. The implementation results suggest that ASE-DMT is more suitable for dimming applications.

INDEX TERMS LiFi; brightness; ASE-DMT; reversed dimming (or PWM dimming); AM dimming; DCO-OFDM; live demonstration; SNR/symbol; FPGA; PXIe-1085; NI-7966R.

I. INTRODUCTION

A. LIFI DEVELOPMENT AND OUR INTEREST

There has been an increase in research and commercial activities in Light Fidelity (LiFi) systems since the first TED Global talk on LiFi in 2011 [1]. The standardization of LiFi is currently being considered by the institute of electrical and electronics engineers (IEEE) 802.11bb task group [2]. The available bandwidth in the visible and short infrared region is 2000 times larger than the whole radio frequency (RF) spectrum. This allows LiFi to be a potential solution for the exponentially increasing demand for wireless access [1]- [2]. Visible light communication (VLC) systems should maintain illumination quality as its primary requirement. For example, light communication systems are all required to have flicker-free illumination. This is highlighted in all light communication standards [3]- [2]. In addition, dimming support is considered as an indispensable feature for VLC systems [3]. Therefore, the illumination quality of VLC systems, particularly brightness dimming, has attracted our research interest.

The standardization of LiFi technology is an essential step in supplying LiFi products to end-users. The physical layer (PHY) and medium access control layer (MAC) are among the main technical details being defined by the IEEE 802.11bb task group on light communication (LC). A brief summary of the dimming support in the currently available IEEE light communication standards is provided in Table 1. Dimming control refers to the capability of a LiFi system to adjust the brightness of a transmitting light source without degrading the performance of the communication link. Several dimming methods have been designed in the IEEE 802.15.7-2011 VLC standard as given in Table 1. These methods are suitable for all the waveforms defined in the PHYs I, II, and III of the standard. However, they result in a degradation in the data rate and the signal-to-noise ratio (SNR). For example, amplitude modulation (AM) dimming reduces the waveform amplitude and thus reduces the SNR, while pulse width modulation (PWM) dimming maintains

TABLE 1. LIGHT COMMUNICATION STANDARDS WITHIN IEEE STANDARDS ASSOCIATION

	PHY layers	Dimming Consideration
IEEE 802.15.7-2011 [4]	PHY I, II, and III are based on rectangular-shape waveform (Pulsed modulation schemes)	Three dimming methods were introduced for VLC waveform (i.e. rectangular waveform), including compensation symbol insertion, pulse width modulation (PWM), and amplitude modulation (AM).
IEEE 802.15.13 [2]	Based on revision of PHY II, III from 802.15.7-2011. OFDM-based LiFi PHY is being added.	Reversed-unipolar LiFi dimming methods (inspired by PWM) can be applied [5]- [6]. However, dimming control is required to be considered for OFDM-based waveforms in the standard to maintain a good communication performance.
IEEE 802.11 TGBB [7]	Based on 802.11 PHYs. Infrared band is mandatory in the wavelength range: (800 nm – 1000 nm).	Dimming method is not yet disclosed; but notice that infrared (IR) is used as mandatory spectrum. Dimming requirements will emerge when the optional visible light spectrum is considered.

a high peak-to-peak voltage but reduces the data rate. AM dimming can be applied to all intensity modulation with direct detection (IM/DD) waveforms. This includes orthogonal frequency division multiplexing (OFDM), which is being introduced in the IEEE 802.15.13 Multi-Gigabit/s Optical Wireless Communications (OWC) Task Group (TG13) and IEEE 802.11 Light-Communication Task Group (TGbb). AM dimming results in an unavoidable performance reduction because it limits the vertical resolution of the analog-to-digital and digital-to-analog converters (ADC/DAC). In contrast, PWM dimming requires a careful design based on the characteristic of the probability density functions (PDF) of the chosen LiFi modulation scheme.

B. IMPLEMENTATION GOALS & CHALLENGES

This paper focuses on the design and implementation of OFDM-based dimming for LiFi systems that does not degrade the communication performance. An off-the-shelf commercial light-emitting-diode (LED) is used because of the LEDs ubiquitous availability. Recent work has shown that choosing an LED can provide over 4 Gbps in data rate [8] by using a 10 GHz clock rate ADC/DAC hardware. The optimization of the bit rate does not fall within the scope of this paper. However, the evaluation of the communication link performance in terms of the measured SNR per symbol (denoted as γ) of the quadrature amplitude modulation (QAM) is considered for a wide range of LED brightness dimming levels. The SNR/symbol, in dB, of an M-QAM, where M is the constellation size, is expressed as:

$$\gamma = 20 \log \left(\frac{u_{QAM}}{\sigma} \right) \quad (1)$$

where u_{QAM} denotes the minimum Euclidean distance of the considered QAM order, and σ denotes the standard deviation of the received QAM symbols relative to the originally transmitted symbols.

The overall goal of the system is to achieve a dimming range between 5% and 95% of the full brightness of the LED and to simultaneously maintain an SNR/symbol above 15 dB for all dimming levels in the brightness range. Augmented spectral efficiency discrete multi-tone (ASE-DMT) is used because it is a spectral and energy efficient modulation scheme [9]–[11]. A hybrid PWM-AM dimming is proposed to be applied to ASE-DMT to enable the dimming control while maintaining the spectral and energy efficiency of ASE-DMT. AM dimming is applied to extend the possible dimming range of the considered modulation schemes. The system is demonstrated on a real-time communication platform. Accordingly, multiple decoders must run in parallel with an acceptable processing delay to provide a live link quality monitoring at each of the layers of multi-layered ASE-DMT [11]. Additionally, the implementation of direct current (DC)-biased optical OFDM (DCO-OFDM) dimming is presented for comparison purposes.

C. AM VS. PWM DIMMING

This paper presents an implementation of a hybrid PWM-AM dimming control based on two modulation schemes: ASE-DMT and DCO-OFDM. The selection of the dimming method is based on the considered dimming level. Figure 1 shows the scaling of the signal amplitude based on the selected dimming levels. The ability to send a larger signal peak-to-peak amplitude is directly linked to achieving a higher SNR. The PWM dimmable range for ASE-DMT is much wider than that of DCO-OFDM given the unipolarity of ASE-DMT waveforms. This is given between 16% and 84% of the full brightness of the considered light source for ASE-DMT. AM is used on top of that to expand the dimming range beyond the capability of PWM (i.e., to reach a dimming range from 5% to 95% brightness). Unfortunately, this results in a controlled degradation in the signal amplitude (i.e. the peak-to-peak voltage), which is unavoidable when AM is applied to dim the waveform. In contrast, the PWM dimming method supports a narrower dimming range for DCO-OFDM (i.e., 25% to 75% brightness) due to the bipolarity of the waveforms. Only half of the signal amplitude range can be used when PWM dimming is applied for DCO-OFDM. Therefore, the reduction in the SNR is unavoidable for DCO-OFDM.

The dimming mechanism in ASE-DMT is mostly based on PWM. This allows ASE-DMT to maintain a better communication performance than DCO-OFDM, as its peak-to-peak amplitude is always higher than that of DCO-OFDM at any applied brightness level. In other words, the PWM dimming-method does not reduce the signal amplitude as illustrated in Figure 1 and therefore the SNR should stay as high as it would if there is no dimming.

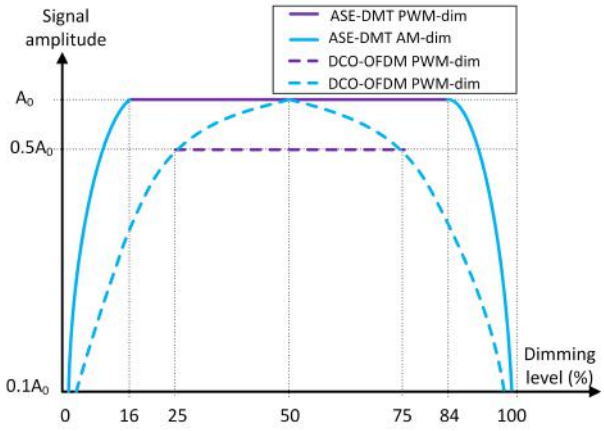

FIGURE 1. An illustration of the modulation signal scaling based on the considered dimming levels.

D. PROPOSED SYSTEM CONFIGURATION

Our implementation is based on a National Instruments (NI) real-time processing platform, e.g., a PXIe-1085 chassis computer, which is equipped with field programmable gate array (FPGA) NI-7966R panels. Each of these panels is operating at 100 MHz clock and can be used for any baseband communication application. A bidirectional direct current (DC)-coupled ADC/DAC, NI-5781, is used for both uplink and downlink with a 20 MHz communication bandwidth. Our initial implementations show the feasibility of achieving data rates of up to 40 Mbps. However the optimization of data rate is not the main objective of this paper. Instead, an evaluation of the communication link performance for the different dimming levels is considered.

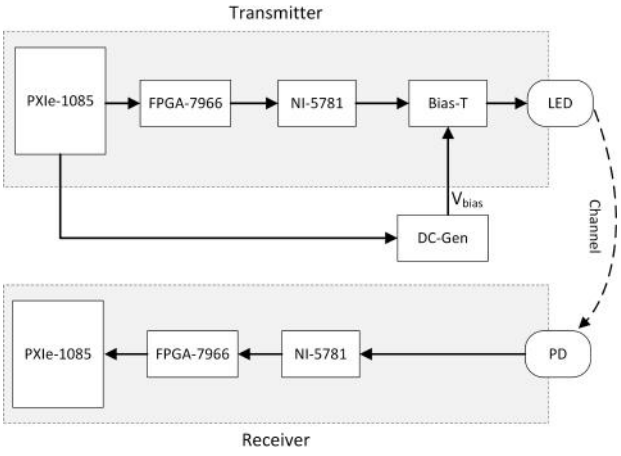

FIGURE 2. System hardware configuration.

Figure 2 shows the used hardware configuration for the proposed system. An off-the-shelf blue LED is used at the transmitter side (Vishay VLMB1500). The used alternative current (AC)-coupled photodetector (PD) (Femto-HSPR-X-I-1G4-SI) has a 1.4 GHz of 3 dB bandwidth. However, the communication bandwidth of 20 MHz is chosen as the upper frequency limit of the used ADC/DAC. By using an AC-coupled bias-T (PSPL5575A), any DC-component of the waveform will be removed after passing the bias-T. Therefore, a programmable DC generator (Keysight E36313A) is connected to the DC input gate of the bias-T to supply the bias voltage to the LED so that the brightness of the LED is controllable by our transmitter software.

II. RELATED WORKS

Multi-tone modulation schemes such as OFDM are popular in LiFi systems as they can maximize the data rate by using adaptive bit and energy loading techniques. Adopting OFDM allows for an inherent multi-user support using OFDM access (OFDMA). In addition, it allows for a faster integration with other OFDM-based RF systems. This is in contrast to pulsed modulation schemes adopted in the IEEE 802.15.7-2011 standard, that offer lower speeds. However, multi-tone waveforms require a different dimming mechanism from that of pulsed modulation schemes. This section compares existing dimming techniques applied to LiFi systems.

The selection of the dimming method depends on the PDF of the waveform. LiFi waveforms can be classed into two categories: (Type I) bipolar waveforms which have a symmetric PDF and a mean value in the centre of the intensity range, and (Type II) unipolar waveforms which have an asymmetric PDF. A typical example of a LiFi waveform type I is DCO-OFDM, while a good example of type II is PAM-DMT [12]. Type II waveforms can be generated by clipping the negative samples of the original bipolar OFDM waveform. The distortion of the zero-level clipping is orthogonal to the information-modulated symbols in all inherent unipolar OFDM schemes [3]. The negative part of the PDF can be ignored without any impact on the receiver (RX). Alternatively, it can be reversed to have a positive value before being transmitted such as in flip-OFDM and unipolar OFDM (U-OFDM) [5] - [13].

A higher SNR is expected to be achieved using type II waveforms in comparison with type I waveforms when compared to the same dynamic range. Unipolar waveforms type II can utilize twice the dynamic range of the bipolar waveforms of type I. That explains, in part, the interest in unipolar LiFi waveforms [14]- [15].

Numerous studies and patents have considered the different dimming methods to control the brightness of the LED during communication, as in [16] - [17]. These works provided interesting simulation results and estimations of spectral efficiency. A real-time implementation of the ASE-DMT transmitter has been recently published [18]. In comparison with the previous works, this paper proposes a hybrid-dimming technique to extend the dimming range of both DCO-OFDM and ASE-DMT. Our implementation of ASE-DMT and DCO-OFDM is more focused on evaluating the dimming capabilities experimentally.

III. IMPLEMENTATION

A. GENERAL DESCRIPTION

A description of the dimming implementation is presented in this section based on ASE-DMT modulation scheme. The implementation of the AM-dimming DCO-OFDM system will not be included. However, it can be simply understood based on this section.

B. TRANSMITTER AND DIMMING CONTROL

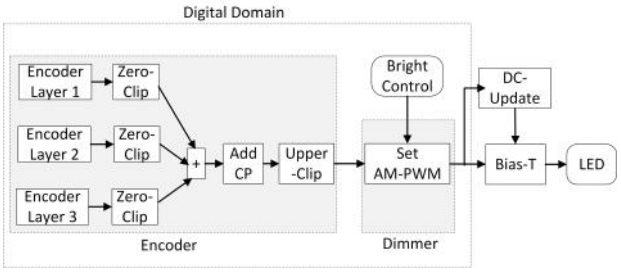

FIGURE 3. ASE-DMT transmitter Block Diagram.

The implementation of a three-layer ASE-DMT transmitter (TX) follows the block diagram in Figure 3. The number of layers is limited to three in this paper as it simplifies the system implementation while at the same time achieving 87.5% of the spectral efficiency of DCO-OFDM. A greater number of layers can be used at the expense of additional memory requirements [11].

AM-PWM dimming and Brightness Control:
There are three parameters to control the brightness in AM-PWM dimming: (1) the bias voltage applied to LED (this is a fixed parameter), (2) the duty cycle of PWM dimming pulse, and (3) the amplitude of the signal (this should be avoided if not necessary as it results in a reduction in the SNR). The dimming process is explained as follows.

Firstly, the modulation layers of ASE-DMT are digitally summed after clipping as:

$$x_{ASE}^{(D)} = \sum_{k=1}^{D} x_{ASE}^{(k)}, \tag{2}$$

where D is the number of modulation layers in the ASE-DMT; k is the index of an individual layer.

Next, one OFDM frame can be assigned to one of two dimming states: a high dimming level (corresponding to the ON duration of the PWM pulse) or a low dimming level (corresponding to the OFF duration). One PWM cycle will be applied to a set of OFDM frames. For example, a set of ten OFDM frames is used in our measurements. PWM will determine the number of OFDM frames that will have a high-dimming level while the remaining ones will have a low dimming level. Let's denote s as the dimming sign applied to an OFDM frame of the sum waveform (denoted as ${x_{ASE}}^{(D)}$). This means that $s = -1$ denotes that the waveform is reversed, while $s = 1$ means the waveform is not. After applying a PWM dimming sign s and a bias voltage (V_{bias}), the modulation waveform is expressed as follows:

$$x_{PWM}^{(D)} = s\left\{\alpha {x_{ASE}}^{(D)}\right\} + V_{bias} \tag{3}$$

where α is the AM scale factor.

After which, the modulation waveform is used to drive an LED which translates it into a fluctuation of optical power, as follows:

$$\begin{aligned} y_{PWM}^{(D)} = f \times x_{PWM}^{(D)} &= f\left\{s\alpha {x_{ASE}}^{(D)} + V_{bias}\right\} \\ &= f\alpha \times s{x_{ASE}}^{(D)} + fV_{bias} \\ &= \alpha \times y_{AC} + y_{bias} \end{aligned} \tag{4}$$

where f denotes the voltage-optical transfer function of the chosen LED. y_{AC} and y_{bias} represents the optical power contributions from the AC signal component and the constant bias voltage (DC component) respectively.

The average optical power (brightness) is calculated in (5). The brightness of an LED can be controlled via the PWM duty cycle, AM scaling of the signal, and the bias voltage of the LED. However, the bias voltage is fixed in our implementation at a constant value while the PWM duty cycle is controlled using our software.

$$\begin{aligned} y_{avg} = E\left\{y_{PWM}^{(D)}\right\} &= E\left\{\alpha \times y_{AC} + y_{bias}\right\} \\ &= \alpha(1-\beta) \times E\left\{{x_{ASE}}^{(D)}\right\} + y_{bias} \\ &= \alpha \times y_{\beta} + y_{bias} \end{aligned} \tag{5}$$

where E is the statistical mean expectation; β is the duty cycle of the PWM dimming signal. y_{β} represents the average optical power contribution from the PWM dimming.

At the receiver side, the optical waveform is received by an AC-coupled photodiode receiver, denoted as $\widehat{y}_{ASE}{}^{(D)}$. This photodiode can ignore the DC components in (4). The channel gain/attenuation factors can also be ignored as they are compensated for in the channel vector estimation. The AC signal component containing the dimming sign s is given as follows:

$$\widehat{y}_{ASE}^{(D)} = s x_{ASE}^{(D)} = s\sum_{k=1}^{D} x_{ASE}^{(k)} \tag{6}$$

Example of dimming:
Without controlling the AM-scaling factor, the OFDM waveform is operating at its maximum amplitude range and the PWM dimmable range is measured to be in between 16% and 84% brightness. When the desired brightness level is outside of the PWM dimming range, the AM dimming method would be applied to reach a lower brightness level. Figure 4 presents some examples of applying different dimming levels on an ASE-DMT waveform using either AM dimming or PWM dimming.

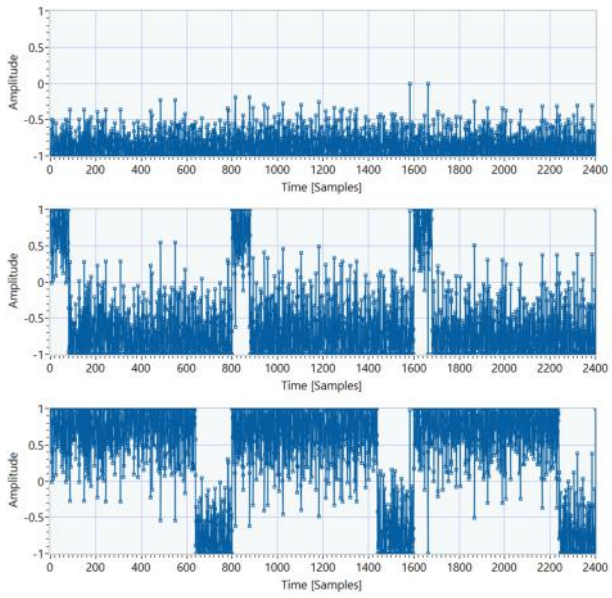

FIGURE 4. Example of dimming control using AM/PWM to target 10%, 30%, and 70% brightness (from the top down).

C. RECEIVER PROCESSING

The block diagram of the receiver and the detailed decoder architecture of ASE-DMT are illustrated in Figure 5 and Figure 6, respectively.

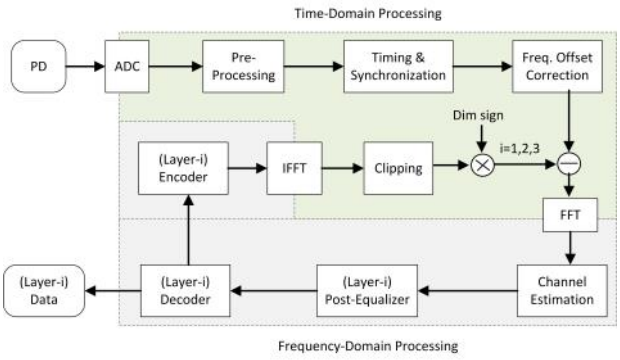

FIGURE 5. Three-layer receiver block diagram.

1) PRE-PROCESSING

Pre-processing techniques such as auto-gain controlling and shot noise removal are applied on the received time-domain samples after they are converted from analog to digital. The processed samples can then be fed into a timing and synchronization process.

2) TIMING AND SYNCHRONIZATION

The system implementation applies a popular timing and synchronization algorithm proposed by Van de Beek et.al for OFDM [19]. The algorithm uses maximum likelihood (ML) optimization to match the start of an OFDM frame and its

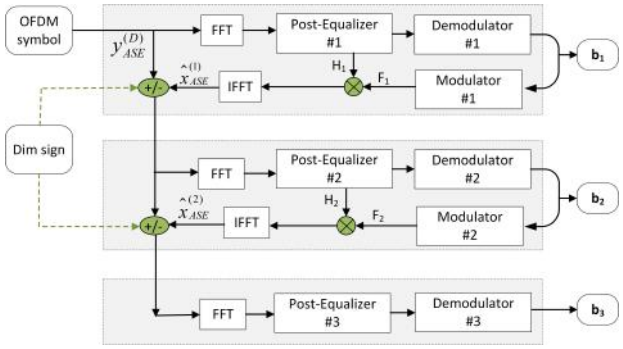

FIGURE 6. Three-layer ASE-DMT decoder.

associated cyclic prefix. However, the algorithm is designed to work with complex-valued RF-based OFDM waveforms. The synchronization algorithm requires some modifications before it can be applied to real-valued optical OFDM waveforms. Our implementation makes two modifications for the different modulation schemes. The first modification pads zeros to the imaginary part of the real-valued waveform. This was experimentally shown to be sufficient for a reliable synchronization in DCO-OFDM. The second modification produces the complexed waveform by merging two adjacent real-valued symbols into a single complex symbol. This was experimentally shown to be sufficient for a reliable synchronization in ASE-DMT. Although both modifications are simple in principle, they are able to provide reliable timing and synchronization to evaluate the link quality. Section VI provides a detailed analysis of these algorithms.

3) PRE-EQUALIZATION VS POST-EQUALIZATION

A training sequence within the PHY header can be used for the time-domain channel estimation and pre-equalization [2]- [7]. The frequency pilots allocated to a few subcarriers can also be used for the post-equalization in the frequency domain. Experimental results have shown that the post-equalization is necessary to correct the phase rotation of the in-phase and Quadrature-phase (IQ) constellations. The pre-equalization can be avoided in ASE-DMT. However, post-equalization is mandatory. Post-equalization at any layer of ASE-DMT with an index k is indispensable as it provides an estimation of the channel matrix H_k. This facilitates the recovery of the time-domain waveform of layer-k that is also used for the decoding of the next layer, as seen in Figure 6.

4) ASE-DMT and PWM dimming sign

This section presents the implications of PWM dimming on a conventional ASE-DMT decoder. A modified decoding process is proposed to mitigate these implications. The following analysis does not take into account the channel scaling factor of the signal amplitude. However, the channel scaling factor is already compensated for during the estimation of the channel matrix H_k. The DC component of the signal will be ignored since ASE-DMT requires minimal turn-on voltage

bias.

In the multi-layer decoding process, we denote that $\widehat{x}_{ASE}{}^{(k)}$ is the estimate of the transmitted $x_{ASE}{}^{(k)}$. This estimation implements a close-loop approximation with an estimated channel vector H_k, (see Figure 6). Next, the input to the decoder at layer-d is denoted as $I^{(d)}$ and calculated as:

$$I^{(d)} = \begin{cases} \widehat{y}_{ASE}{}^{(D)} & \text{if } d = 1, \\ I^{(1)} - s\sum_{k=1}^{d-1} \widehat{x}_{ASE}{}^{(k)} & \text{if } d > 1. \end{cases} \tag{7}$$

The inputs at decoding layers are also expressed in a recursion form:

$$I^{(d)} = I^{(d-1)} - s \times \widehat{x}_{ASE}{}^{(d-1)}. \tag{8}$$

Finally, the recursive subtraction in Equation 8 will result in a simple form of the inputs at decoding layers in (9). It clearly shows the dependence of the dimming sign on the input to the demodulation layers.

$$I^{(d)} = s\sum_{k=d}^{D} \widehat{x}_{ASE}{}^{(k)} \tag{9}$$

Any inaccurate dimming sign at a particular ASE-DMT layer results in an incorrect recovery of the OFDM symbols at the next layer. This leads to a cascade of erroneous decoding at all subsequent layers due to the propagation of errors. the transmitter is designed to send a data frame to inform the receiver of the current brightness level and the sequence of the dimming signs that are going to be used in the next payload. This follows the dimming mechanism introduced by the IEEE 802.15.7-2011 standard. Then, the receiver can look up for the dimming-sign sequence in order to achieve a successful decoding of the incoming waveforms.

D. BRIGHTNESS CONTROL TO OPTICAL POWER CONVERSION

Figure 7 presents the measured optical power at the different considered dimming levels. This shows a conversion between our software-based custom brightness control value (in percent) and the actual optical power (in milli-Watt). The measurement was performed using the optical power meter PM100USB and S121C photodiode power sensor.

IV. RESULTS AND DISCUSSION

The SNR per symbol is measured continuously for each of the received frames. For a fair evaluation of link quality between DCO-OFDM and ASE-DMT, the implementation results are all measured under the same clipping factor and channel conditions.

In the ASE-DMT implementation, there are three layers as discussed in the previous section. The SNR/symbol values at each of the three layers are measured. The experimental results revealed that there is a SNR/symbol reduction of 1dB to 3dB between the lower and higher-order layers

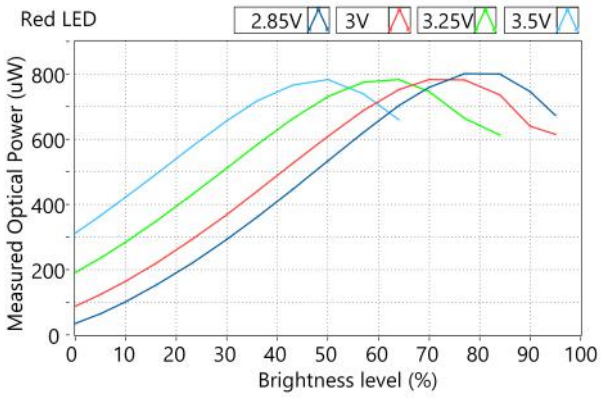

FIGURE 7. Measured optical power response at different controlled brightness levels.

due to the error propagation. However, this reduction of the SNR/symbol per layer is nearly constant during the considered dimming range. For the purpose of comparison with DCO-OFDM, a normalized SNR/symbol value (γ_{ASE}) for all ASE-DMT layers is calculated based on the spectral efficiency contribution of each layer as follows:

$$\gamma_{ASE} = \sum_{d=1}^{D} 10^{\gamma_d/10} \times \frac{2^{-(d-1)}}{2 - 2^{-(D-1)}}, \tag{10}$$

where D is the number of modulation layers in ASE-DMT, d is the index of each layer, and γ_d denotes the measured SNR/symbol values at the layer indexed d.

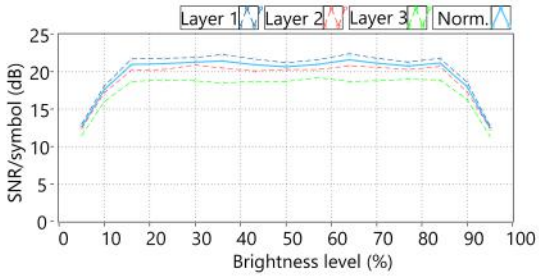

FIGURE 8. Normalization of measured SNR/symbol at three layers of ASE-DMT.

Figure 8 presents the normalized and the measured SNR/symbol values for the three layer ASE-DMT waveform. The normalized curve is closer to the values of layer 1 because of its higher spectral contribution relative to the other layers. In order for the comparison between ASE-DMT and DCO-OFDM to be more clear, the normalized results for ASE-DMT are only presented for the rest of this paper.

For a fair performance comparison, the performance of DCO-OFDM and ASE-DMT is measured at the same spectral efficiency levels. Particularly, the performance of 4-QAM

DCO-OFDM is compared with that of 2-PAM ASE-DMT, while 16-QAM DCO-OFDM is compared with 4-PAM ASE-DMT.

A. BACK-TO-BACK LINK

A direct back-to-back (B2B) link is tested to investigate the decoder behaviour and the maximum SNR/symbol performance that can be afforded by the used hardware. In addition, this measurement helps us to validate the operation of the entire communication system.

1) 4-QAM DCO-OFDM VS. 2-PAM ASE-DMT

Figure 9 shows the measured SNR/symbol results of 2-PAM ASE-DMT and 4-QAM DCO-OFDM for all dimming values between 5% and 95%. The signal amplitude is scaled-down 20 times to simulate the attenuation effect on the received signal. The best performance that the system can afford in the B2B link is measured at a 30 dB SNR/symbol. The SNR/symbol will not exceed 40 dB in the case where the signal is directly sent without any amplitude scaling. The clipping distortion, non-ideal filtering of the DC component and ADC/DAC quantization noise are the main factors in limiting the SNR/symbol.

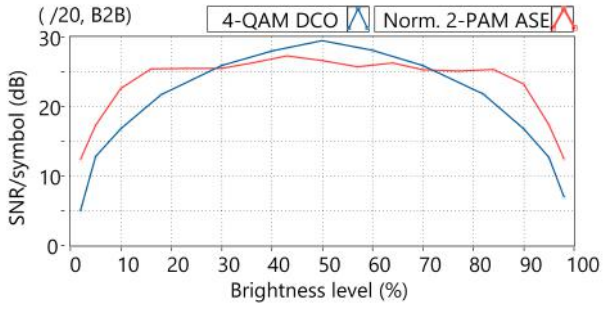

FIGURE 9. Measured SNR/symbol in B2B System (4-QAM DCO-OFDM versus 2-PAM ASE-DMT) by using a 20-times attenuator.

The measured results in Figure 9 show the effect of dimming on the system performance at different brightness levels. It is shown that the performance of DCO-OFDM reaches its maximum at a brightness level of 50%. This is the brightness level where the peak-to-peak amplitude of DCO-OFDM is the highest as shown in Figure 1. The performance of ASE-DMT is relatively constant for the dimming levels in-between its PWM dimmable range (i.e., 16% and 84% in brightness).

The performance of 2-PAM ASE-DMT is nearly constant around 25 dB within its PWM dimming range. However, it is 3 dB lower than the peak performance of 4-QAM DCO-OFDM at 50% dimming. This is reasonable due to the error propagation between the layers of ASE-DMT. However, at the boundaries of the PWM dimming range, ASE-DMT outperforms DCO-OFDM by around 5 dB. Moreover, for all the other dimming levels in the low brightness range (less than 16% in brightness) or in the high brightness range (greater than 84% in brightness), ASE-DMT outperforms DCO-OFDM by 6 dB SNR/symbol.

2) 16-QAM DCO-OFDM VS. 4-PAM ASE-DMT

Figure 10 presents the measured SNR/symbol values of 4-PAM ASE-DMT and 16-QAM DCO-OFDM for brightness levels between 5% and 95%. The results are also measured when the signal amplitude is scaled-down by 20-times to simulate the channel attenuation as discussed earlier.

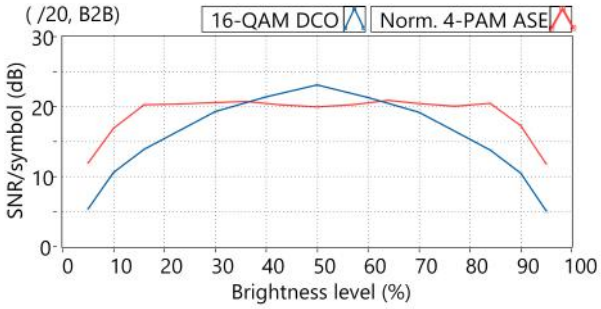

FIGURE 10. Measured SNR/symbol in B2B System (16-QAM DCO-OFDM versus 4-PAM ASE-DMT) by using a 20-times attenuator.

The change of the measured SNR/symbol in Figure 10 follows the amplitude scaling that is shown in Figure 1. DCO-OFDM reaches its peak performance of 23.5 dB at a dimming level of 50%, while ASE-DMT achieves a relatively constant SNR/symbol of 20 dB for all the dimming levels between 16% and 84%. A significant gain of around 6 dB from ASE-DMT over DCO-OFDM is shown at the boundaries of the PWM dimming range (i.e., 16 and 84% brightness levels). The SNR/symbol gain of ASE-DMT over DCO-OFDM is maintained for all the dimming levels outside the PWM dimming range.

The expected constant and high SNR/symbol of ASE-DMT within the PWM dimming levels is now experimentally proven. Significantly, the results highlight that ASE-DMT can achieve a high performance under low dimming conditions. ASE-DMT outperforms DCO-OFDM for all dimming levels lower than 30% or higher than 70%.

B. OPTICAL LINK

The results of the back-to-back link show that ASE-DMT is the preferred scheme at the low and high dimming levels. In a practical optical link, the SNR/symbol gain of ASE-DMT changes based on the selection of the bias voltage of the LED. Detailed results are presented in the following sections.

1) 4-QAM DCO-OFDM VS. 2-PAM ASE-DMT

The selection of the bias voltage applied to the LED has a significant impact on the communication performance due

to the nonlinear voltage-intensity response of the LED. The turn-on voltage for the used red LED is around 1.8V. This bias voltage represents the case of an entire-OFF voltage for the LED as it results in low optical power. In addition, a bias voltage which is close to the LED turn-on voltage results in significant distortion for the AC modulating waveform. This comes from the nonlinear V-I characteristic of LED. In the experiment, we selected a bias voltage higher than 2.8V to generate a signal output within the dynamic range of the chosen LED.

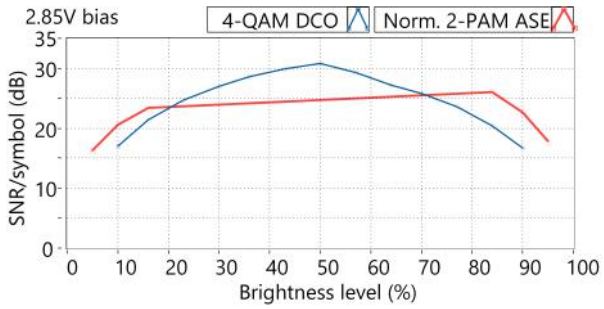

FIGURE 11. Measured SNR/symbol in Optical Link (4-QAM DCO-OFDM versus 2-PAM ASE-DMT); 2V peak-to-peak voltage applied to a 2.85V bias.

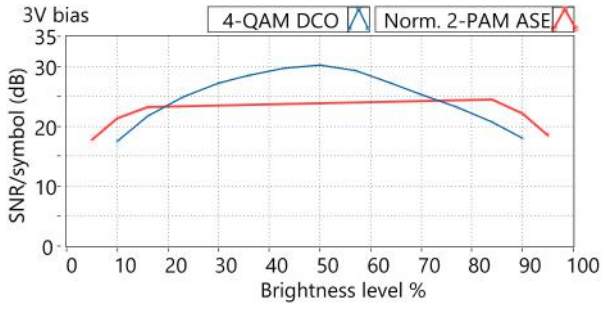

FIGURE 12. Measured SNR/symbol in Optical Link (4-QAM DCO-OFDM versus 2-PAM ASE-DMT); 2V peak-to-peak voltage applied to a 3.0V bias.

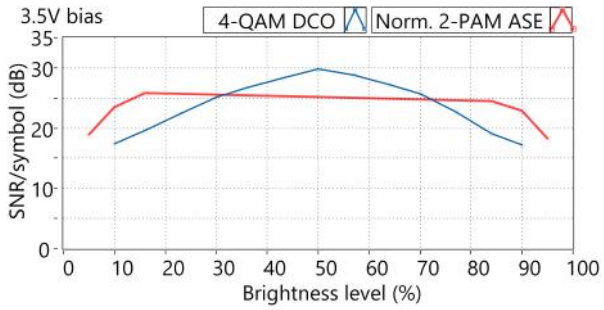

FIGURE 13. Measured SNR/symbol in Optical Link (4-QAM DCO-OFDM versus 2-PAM ASE-DMT); 2V peak-to-peak voltage applied to a 3.5V bias.

When different bias voltages of 2.85V, 3V, and 3.5V are applied, the SNR/symbol differs by a few dB in the marginal transition between PWM dimming and AM dimming. Particularly, the SNR/symbol is lower when the bias voltage is low. In all results, 2-PAM ASE-DMT achieves a SNR/symbol of 26 dB, while 4-QAM DCO-OFDM reaches a peak of 30 dB at a brightness level of 50%. ASE-DMT achieves around 25 dB for all of its PWM dimming range while the DCO-OFDM performance peaks at 50% dimming level and monotonically decreases at higher and lower dimming levels. Consequently, ASE-DMT outperforms DCO-OFDM for most of the low dimming levels, such as all brightness levels lower than 20% in the case of 2.85V and 3V bias voltage (Figures 11 and 12), and lower than 30% in the case of 3.5V (Figure 13). Similarly, the SNR/symbol gain of ASE-DMT over DCO-OFDM can be seen when its dimming level is higher than 70% for all the considered bias voltages.

The advantage of using ASE-DMT is more pronounced when a bias voltage of 3.5V is selected as shown in Figure 13. A significant gain of around 6 dB is seen for ASE-DMT over DCO-OFDM at the brightness boundaries of the PWM dimming range (16% and 84%). Especially at extremely low and high dimming levels (5% or 95%), DCO-OFDM shows its worst performance while ASE-DMT can still maintain a SNR/symbol of more than 15 dB.

2) 16-QAM DCO-OFDM VS. 4-PAM ASE-DMT

The advantages of ASE-DMT in comparison with DCO-OFDM are still present when comparing 4-PAM ASE-DMT with 16-QAM DCO-OFDM at low bias voltages of 2.85V and 3V, as shown in Figures 14 and 15. The gain of ASE-DMT over DCO-DMT (up to 3 dB) can only be seen at low dimming levels that are less than 16% in brightness. At these low bias voltages, the lower part of the ASE-DMT waveform is distorted and the SNR/symbol performance gain diminishes. ASE-DMT offers a significant 5 dB gain in the SNR/symbol over DCO-OFDM at high dimming levels (greater than 84%).

The improvements of ASE-DMT in comparison with DCO-OFDM are also present for dimming levels outside the range between 25%-75% when a high bias voltage of 3.5V is applied as shown in Figure 16. Another notable highlight of ASE-DMT is that it can reach extremely low or high dimming levels (5% and 95%) and still maintain an acceptable performance (with the SNR/symbol above 12 dB).

Overall, ASE-DMT is more suitable for dimming in comparison with DCO-OFDM because of its constantly high performance and its low brightness support. The maximum SNR/symbol advantage of ASE-DMT over DCO-OFDM is between 2 dB and 7 dB if 2-PAM is used, and from 1 dB to 6 dB if 4-PAM is used. Unlike the B2B performance in Section IV-A, this practical gain changes according to the selection of the bias voltage and the dimming level.

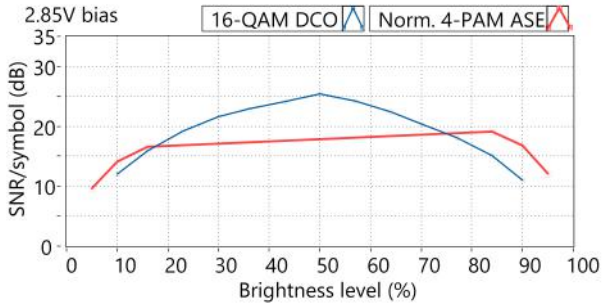

FIGURE 14. Measured SNR/symbol in Optical Link (16-QAM DCO-OFDM versus 4-PAM ASE-DMT); 2V peak-to-peak voltage applied to a 2.85V bias.

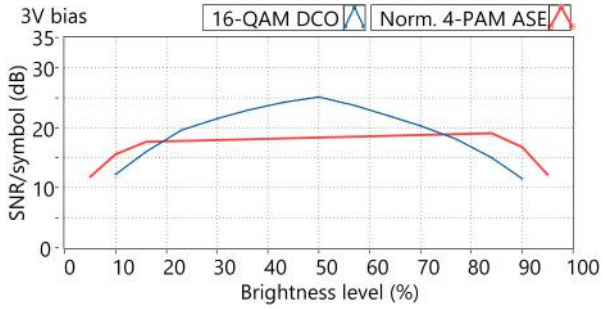

FIGURE 15. Measured SNR/symbol in Optical Link (16-QAM DCO-OFDM versus 4-PAM ASE-DMT); 2V peak-to-peak voltage applied to a 3.0V bias.

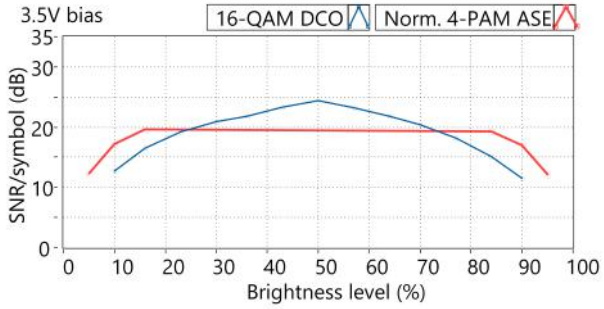

FIGURE 16. Measured SNR/symbol in Optical Link (16-QAM DCO-OFDM versus 4-PAM ASE-DMT); 2V peak-to-peak voltage applied to a 3.5V bias.

V. CONCLUSION

Several analyses have been presented to explain the implementation of the proposed dimming systems. Different dimming methods (AM dimming, PWM dimming, and hybrid dimming methods) were implemented for DCO-OFDM and ASE-DMT modulation schemes. Practical comparisons in terms of the link quality of different dimming methods are presented.

Practical measurement results show that the PWM dimming method provides a high performance within its supported brightness range. Particularly, ASE-DMT achieved a nearly constant SNR/symbol of up to 25 dB within its wide PWM dimming range (between 16% and 84% brightness). In contrast, AM dimming degrades the communication quality of both DCO-OFDM and ASE-DMT. However, a measured SNR/symbol of 15 dB can be guaranteed when AM dimming is additionally applied to extend the dimming range of ASE-DMT to be between 5% and 95%.

When comparing the two modulation schemes, ASE-DMT outperforms DCO-OFDM at low brightness levels (i.e., all dimming levels below 20% brightness), thus ASE-DMT is better than DCO-OFDM for targeting low optical power applications.

REFERENCES

[1] Harald Haas: Wireless data from every light bulb, TED Global, Aug. 2011.
[2] IEEE 802.15 WPAN Task Group 13 (TG13) Multi-Gigabit/s Optical Wireless Communications, IEEE Standards Association Std.
[3] M. S. Islim and H. Haas, "Modulation techniques for li-fi," ZTE Communication, vol. 14, pp. 29–40, 2016.
[4] S. Rajagopal, R. Roberts, and S.-K. Lim, "Ieee 802.15.7 visible light communication: Modulation schemes and dimming support," IEEE Commun. Mag., vol. 50, no. 3, p. 72–82, 2012.
[5] N. Fernando, Y. Hong, and E. Viterbo, "Flip-ofdm for unipolar communication systems," IEEE Transactions on Communications, vol. 69, no. 12, pp. 3726–3733, 2012.
[6] S. D. Dissanayake and J. Armstrong, "Comparison of aco-ofdm, dco-ofdm and ado-ofdm in im/dd systems," Journal of Lightwave Technology, vol. 31, no. 7, pp. 1063–1072, 2013.
[7] IEEE Standards Association: EEE 802.11 –Light Communication (LC) Task Group (TG) –Meeting update, IEEE Standards Association Std.
[8] R. Bian, I. Tavakkolnia, and H. Haas, "15.73 gb/s visible light communication with off-the-shelf leds," Journal of Lightwave Technology, vol. 37, no. 10, pp. 2418–2424, 2019.
[9] M. S. Islim and H. Haas, "Augmenting the spectral efficiency of enhanced pam-dmt-based optical wireless communications," Opt. Express, vol. 24, no. 11, pp. 11 932–11 949, May 2016. [Online]. Available: http://www.opticsexpress.org/abstract.cfm?URI=oe-24-11-11932
[10] M. S. Islim and H. Haas, "An experimental demonstration of an energy efficient dmt technique for lifi systems," in 2019 IEEE International Conference on Communications Workshops (ICC Workshops), 2019, pp. 1–5.
[11] M. S. Islim and H. Haas, "Communication scheme for intensity modulated systems," US Patent US20 190 253 148A1, 2019. [Online]. Available: https://patents.google.com/patent/US20190253148A1/en
[12] S. C. J. Lee, S. Randel, F. Breyer, and A. M. J. Koonen, "Pam-dmt for intensity-modulated and direct-detection optical communication systems," IEEE Photonics Technology Letters, vol. 21, no. 23, pp. 1749–1751, 2009.
[13] D. Tsonev, S. Sinanovic, and H. Haas, "Novel unipolar orthogonal frequency division multiplexing (u-ofdm) for optical wireless," in 2012 IEEE 75th Vehicular Technology Conference (VTC Spring), 2012, pp. 1–5.
[14] J. Zhou and W. Zhang, "A comparative study of unipolar ofdm schemes in gaussian optical intensity channel," IEEE Transactions on Communications, pp. 1549–1564, 2018.
[15] A. A. W., L. G. Yannis, and G. Maury, "Performance analysis of precoded layered aco-ofdm for visible light communication systems," Optical Communications, vol. 440, pp. 49–60, 2019.
[16] X. Zhang, Q. Wang, R. Zhang, S. Chen, and L. Hanzo, "Performance analysis of layered aco-ofdm," IEEE Access, vol. 5, pp. 18 366–18 381, 2017.
[17] Z. Yang, M. Jiang, L. Zhang, and H. Tan, "Enhanced multiple pulse position modulation aided reverse polarity optical ofdm system with extended dimming control," IEEE Photonics Journal, vol. 10, no. 3, pp. 1–17, 2018.
[18] Q. Wang, B. Song, B. Corcoran, L. Zhuang, and A. J. Lowery, "Real-time demonstration of augmented-spectral-efficiency dmt transmitter using a single ifft," Journal of Lightwave Technology, vol. 35, no. 21, pp. 4796–4803, 2017.
[19] J. J. van de Beek, M. Sandell, and P. O. Borjesson, "Ml estimation of time and frequency offset in ofdm systems," IEEE Transactions on Signal Processing, vol. 45, no. 7, pp. 1800–1805, 1997.

[20] Y. Sun, F. Yang, and J. Gao, "Comparison of hybrid optical modulation schemes for visible light communication," IEEE Photonics Journal, vol. 9, no. 3, pp. 1–13, 2017.

TRANG NGUYEN earned Biomedical Engineering degree from Hanoi Univ. of Science & Technology (HUST), Vietnam in 2013; M.Sc. and PhD. degrees in Electrical & Electronics Engineering from Kookmin University (KMU), South Korea in 2015 and 2018 respectively.
His research interests mainly focus on the physical layer of Optical Wireless Communications. He had been an active member and voting member of IEEE 80.15.7m Task Group within IEEE standards association (IEEE-SA) from 2015 to 2018. Currently, he is a research associate at LiFi Research and Development Center, the University of Edinburgh.

MOHAMED SUFYAN ISLIM received his MSc (Distinction) in communications engineering from Aleppo University, Syria in 2013. Among several scholarships he received in 2013, he was awarded the Global Edinburgh Syrian Scholarship from Edinburgh University. He received both his MSc in signal processing and communications and his PhD in Digital Communications from The University of Edinburgh, UK in 2014 and 2019, respectively. In addition, he received the IEEE communications chapter prize for the best MSc project in 2014. He has co-authored 11 conference papers, 14 journal papers, 2 book chapters and 2 pending patents. He is currently a Post-doctoral Research Associate at the LiFi Research and Development Centre, University of Edinburgh. His main research interests include optical OFDM, LiFi, and optical wireless communications.

HARALD HAAS (Fellow, IEEE) received the Ph.D. degree from The University of Edinburgh in 2001. He is currently the Chair of Mobile Communications at The University of Edinburgh, and he is the Initiator, Co-Founder, and Chief Scientific Officer of pureLiFi Ltd., and the Director of the LiFi Research and Development Centre, The University of Edinburgh. He has authored 500 conference and journal papers. His main research interests are in optical wireless communications, hybrid optical wireless and RF communications, spatial modulation, and interference coordination in wireless networks. He is an Associate Editor of the IEEE Journal of Lightwave Technologies. He gave two TED Global talks "Wireless Data From Every light Bulb" and "Forget Wi-Fi: Meet the New Li-Fi Internet" which together have been downloaded more than 5.5 million times. In 2012 and 2017, he was a recipient of the prestigious Established Career Fellowship from the Engineering and Physical Sciences Research Council (EPSRC) in the U.K. In 2014, he was selected by EPSRC as one of ten Recognizing Inspirational Scientists and Engineers Leaders in the U.K. He was a co-recipient of the EURASIP Best Paper Award for the Journal on Wireless Communications and Networking in 2015 and the Jack Neubauer Memorial Award of the IEEE Vehicular Technology Society. In 2016, he received the Outstanding Achievement Award from the International Solid State Lighting Alliance. He was a co-recipient of recent best paper awards at VTC-Fall, 2013, VTC-Spring 2015, ICC 2016, ICC 2017 and ICC 2018. In 2019 he received the James Evans Avant Garde Award of the IEEE Vehicular Technology Society. Haas is a Fellow of the Royal Academy of Engineering.

VI. ANNEX 1: THEORETICAL ANALYSIS

This section provides a theoretical analysis for the proposed PWM dimming ASE-DMT system. Throughout this section, the effect of clipping on the communication performance is analysed in Subsection VI-A. The analysis of the PDF of ASE-DMT layers and the sum waveform is presented in Subsection VI-B. Afterwards, the measurement of the PWM dimming range is presented in the next subsection. Finally, Subsection VI-D explains the proposed synchronization algorithm.

A. CLIPPING-FACTOR VERSUS SNR-PER-SYMBOL

The modulated signals at individual layers of ASE-DMT apply a zero-level clipping process to remove the negative part of the waveform. This zero-clipping process generates the unipolar characteristic for the ASE-DMT waveform. In addition, upper-level clipping is required to reduce the peak-to-average power ratio (PAPR). However, the upper-clipping certainly influences the communication. An optimal value for the clipping factor is objective in this experimental investigation.

Figures 17 and 18 present the SNR/symbol at demodulation layers 1, 2, and 3 changing as a function of the upper clipping factor. The simulation performances at different channel conditions, a noise-free and an 28 dB SNR channels, are shown. The channel without noise tests the maximum performance the system can afford, that is influenced by the clipping noise; thus the link quality increases when the clipping factor increases. However, under the presence of white noise (particularly 28 dB SNR channel), either a low or a high clipping factor reduces the performance of the demodulation layers. Accordingly, the results show that the clipping factor of 2.5 is optimal for achieving the best performance in both cases of 2-PAM and 4-PAM in the noisy channel. This optimal value for clipping factor varies according to the channel SNR, and it should be practically investigated.

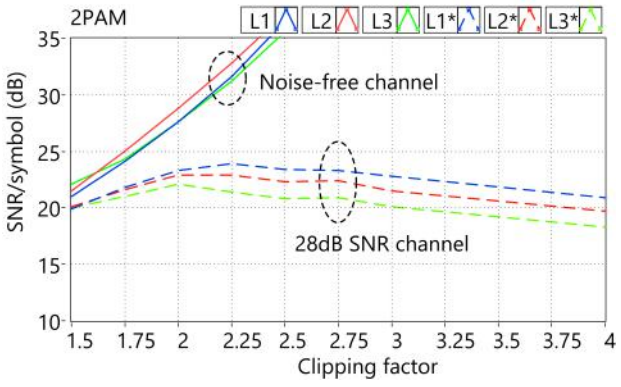

FIGURE 17. Simulated SNR/symbol versus clipping factor in 2-PAM ASE-DMT.

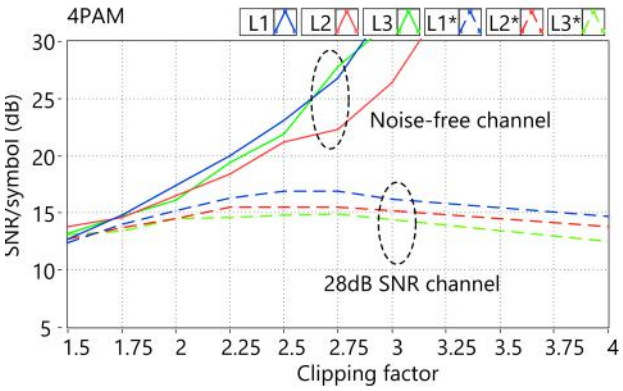

FIGURE 18. Simulated SNR/symbol versus clipping factor in 4-PAM ASE-DMT.

B. PDF ANALYSIS

The analysis of the PDF profile is provided to analysis the PWM dimming capability of ASE-DMT waveform. Notice that the unclipped output of an Inverse Fast Fourier Transform (IFFT) before adding a cyclic prefix (CP) is a Gaussian process [19]. Without loss of generality, the effect of CP addition is not considered for this analysis for simplicity.

1) PDF OF INDIVIDUAL LAYERS

PDF estimation:

The PDF of a PAM-modulated OFDM signal in the time domain at the d-th layer follows a clipped Gaussian distribution. The PDF for the signal at layer d, denoted as $f_{x^{(d)}{}_{ASE}}$ is givenn as follows [15]:

$$f_{x^{(d)}{}_{ASE}} = \frac{1}{\sqrt{2\pi}\sigma_d}\exp(\frac{-\omega^2}{2\sigma_d^2})u(\omega) + \frac{1}{2}\delta(\omega), \omega \in \mathbb{R}. \tag{11}$$

This can be simplified [16] as follows:

$$f_{x^{(d)}_{ASE}}(\omega, \sigma_d) = \Theta(\omega, \sigma_d^2)u(\omega) + \frac{1}{2}\delta(\omega), \omega \in \mathbb{R}, \tag{12}$$

where σ_d is the root mean square (RMS) of the unclipped signal at layer d; $\delta(\omega)$ is the Dirac delta function; and $u(\omega)$ refers to the unit step function. $\Theta(\omega, \sigma_d^2)$ denotes the PDF of a zero-mean Gaussian distribution.

Mean and Variance:

The following estimations are based on Zhang et. al., [16]. The standard deviation of the d-th layer waveform is calculated as follows:

$$E\left\{\left[x_{ASE}{}^{(d)}\right]^2\right\} = \int_{-\infty}^{\infty} z^2 f_{x^{(d)}{}_{ASE}}(z, \sigma_d)dz$$

$$= \int_{-\infty}^{\infty}\left[z^2\Theta(\omega, \sigma_d^2)u(z) + \frac{1}{2}z^2\delta(z)\right]dz = \frac{\sigma_d^2}{2}. \tag{13}$$

The average amplitude of the clipped signal can be calculated as $E\{x_{ASE}^{(d)}\} = \sigma_d/\sqrt{2\pi}$; while the standard deviation of the signal at the d-th layer is denoted as $E[x_{ASE}^{(d)}]^2$. We note that the relationship between the standard deviation of the signals at different layers is given as $\sigma_d^2 = 2^{d-1}\sigma_1^2$.

The mean of the waveform $x_{ASE}^{(d)}$ at layer d can then be given as:

$$\begin{aligned} E\left\{{x_{ASE}}^{(d)}\right\} &= \int_{-\infty}^{\infty} z f_{{x^{(d)}}_{ASE}}(z, \sigma_d) dz \\ &= \int_{-\infty}^{\infty} [z\Theta(\omega, \sigma_d^2)u(z) + \frac{1}{2}z\delta(z)]dz \\ &= \frac{\sigma_d}{\sqrt{2\pi}} = \frac{\sigma_1}{2^{(d/2)}\sqrt{\pi}}. \end{aligned} \quad (14)$$

The variance of the signal at layer d, $x_{ASE}^{(d)}$, can then be given as follows:

$$\begin{aligned} D\left\{{x_{ASE}}^{(d)}\right\} &= E\left\{\left[{x_{ASE}}^{(d)}\right]^2\right\} - E^2\left\{{x_{ASE}}^{(d)}\right\} \\ &= \frac{\sigma_d^2}{2} - \left\{\frac{\sigma_1}{2^{(d/2)}\sqrt{\pi}}\right\}^2 = \frac{\pi - 1}{2^d \pi}\sigma_1^2 \end{aligned} \quad (15)$$

2) ACCUMULATE PDFS

PDF estimation:

The PDF of the summed ASE-DMT layer can be obtained by the convolution of the PDFs of different layers. This is given as follows [20]:

$$f_{{y^{(D)}}_{ASE}} = f_{{x^{(d=1)}}_{ASE}} \otimes f_{{x^{(d=2)}}_{ASE}} \otimes \ldots \otimes f_{{x^{(d=D)}}_{ASE}} \quad (16)$$

where $\otimes$ represents the convolutional operator.

The relationship between the standard deviation values at different layers $\sigma_1, \sigma_2 = \sigma_1/\sqrt{2}, \sigma_3 = \sigma_1/2$ have been taken into account in deriving the PDF of ASE-DMT. Based on (16), the PDF analysis for two-layer and three-layer ASE-DMT is given in the (19) to (21) [20].

Mean and variance:

The mean and variance for the superposition ASE-DMT waveform are derived [16] as follows:

$$\begin{aligned} E_D\left\{{y_{ASE}}^{(D)}\right\} &= E\left\{\sum_{d=1}^{D} {x_{ASE}}^{(d)}\right\} \\ &= \sum_{d=1}^{D} \frac{\sigma_1}{2^{(d/2)}\sqrt{\pi}} = \left\{\frac{1 - 2^{D/2}}{\sqrt{2} - 1}\right\}\frac{\sigma}{\sqrt{\pi}} \end{aligned} \quad (17)$$

TABLE 2. REAL TRANSMITTER OUTPUT VERSUS THEORETICAL MODEL

	Layer 1	Layer 2	Layer 3	Sum L1+L2	Sum L1+L2+L3
Mean (measured)	0.03	0.02	0.02	0.06	0.08
Mean (model)	0.036	0.025	0.018	0.061	0.079

$$\begin{aligned} D_D\left\{{y_{ASE}}^{(D)}\right\} &= D\left\{\sum_{d=1}^{D} {x_{ASE}}^{(d)}\right\} \\ &= \sum_{d=1}^{D} \frac{\pi - 1}{2^d \pi}\sigma_1^2 = (1 - \frac{1}{2^D})(\frac{\pi - 1}{\pi})\sigma_1^2 \end{aligned} \quad (18)$$

Table 2 compares the numerical results of the theoretical analysis and the measured parameters at the output of our ASE-DMT transmitter. There is a tolerance for the difference between the model and the real transmitter output. The decoders in our implementation did not allocate the entire subcarriers for the transmitted data. The encoders deactivated several subcarriers near the DC frequency while some other subcarriers were used to carry the pilot symbols. Additionally, the chosen FFT size of 64 makes the PDF profiles less statistically significant to be compared with theoretical analysis. The upper clipping process applied to the output of the decoders reduces PAPR which results in additional difference between the theoretical and practical mean values.

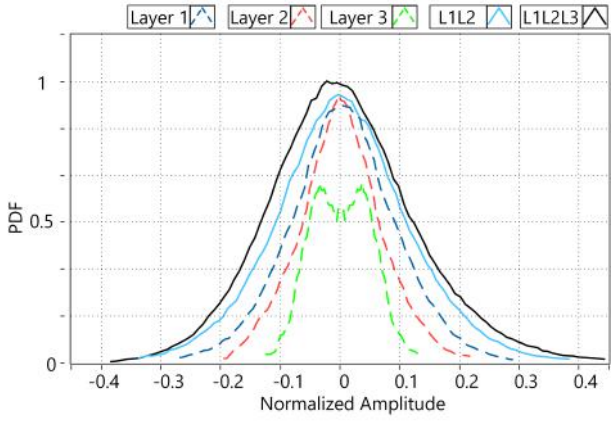

FIGURE 19. Unclipped PDF of layers (L1, L2, L3) and the sum waveforms (L1+L2 and L1+L2+L3).

Figures 19-21 shows the experimentally obtained PDFs at layers 1-3 and the summed ASE-DMT waveform. It is noticed that the PDF of layer 3 is different to that of the first two layers. This is due to the sparsity of the selective loading of higher order layers in ASE-DMT. In fact, there

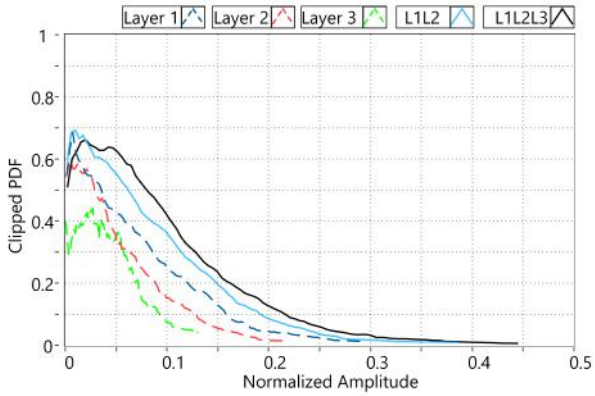

FIGURE 20. Clipped PDF of layers (L1, L2, L3) and the sum waveforms (L1+L2 and L1+L2+L3) (DC component is ignored).

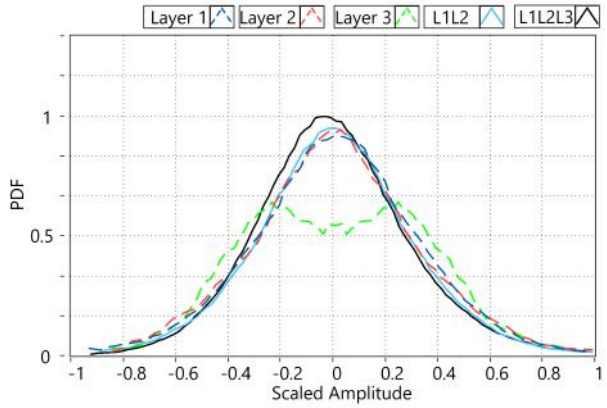

FIGURE 21. Scaled profiles of unclipped PDFs.

are only a few subcarriers at layer 3 that carries data. From our simulations, the PDFs of all layers become similar when the FFT size increases to be greater than 128.

$$f_{y^{(2)}{}_{ASE}}(\omega) = f_{x^{(1)}{}_{ASE}} \otimes f_{x^{(2)}{}_{ASE}}$$

$$= \int_{-\infty}^{\infty} \left[\frac{1}{\sqrt{2\pi}\sigma_1} \exp(\frac{-k^2}{2\sigma_1^2}) u(k) + \frac{1}{2}\delta(k) \right] \left[\frac{1}{\sqrt{2\pi}\sigma_1} \exp(\frac{-(\omega-k)^2}{2\sigma_2^2}) u(\omega-k) + \frac{1}{2}\delta(\omega-k) \right] d_k$$

$$= [\frac{1}{\sqrt{2\pi(\sigma_1^2+\sigma_2^2)}} \exp(\frac{-(\omega)^2}{2(\sigma_1^2+\sigma_2^2)}) \times \left[Q\left(\frac{-\sigma_1\omega}{\sigma_2\sqrt{\sigma_1^2+\sigma_2^2}} \right) - Q\left(\frac{-\sigma_2\omega}{\sigma_1\sqrt{\sigma_1^2+\sigma_2^2}} \right) \right]$$

$$+ \frac{1}{2\sqrt{2\pi}} \left[\frac{1}{\sigma_1} \exp(\frac{-\omega^2}{2\sigma_1^2}) + \frac{1}{\sigma_2} \exp(\frac{-\omega^2}{2\sigma_2^2}) \right] u(\omega) + \frac{1}{4}\delta(\omega) \tag{19}$$

$$f_{y^{(3)}{}_{ASE}}(\omega) = f_{x^{(1)}{}_{ASE}} \otimes f_{x^{(2)}{}_{ASE}} \otimes f_{x^{(3)}{}_{ASE}}$$

$$= \frac{1}{4\sqrt{2\pi(\sigma_1^2+\sigma_2^2)}} \exp(\frac{-\omega^2}{2(\sigma_1^2+\sigma_2^2)}) \times \left[Q\left(\frac{-\sigma_2\omega}{\sigma_1\sqrt{\sigma_1^2+\sigma_2^2}} \right) - Q\left(\frac{-\sigma_1\omega}{\sigma_2\sqrt{\sigma_1^2+\sigma_2^2}} \right) \right] u(\omega)$$
$$+ \frac{1}{4\sqrt{2\pi(\sigma_1^2+\sigma_3^2)}} \exp(\frac{-\omega^2}{2(\sigma_1^2+\sigma_3^2)}) \times \left[Q\left(\frac{-\sigma_3\omega}{\sigma_1\sqrt{\sigma_1^2+\sigma_3^2}} \right) - Q\left(\frac{-\sigma_1\omega}{\sigma_3\sqrt{\sigma_1^2+\sigma_3^2}} \right) \right] u(\omega)$$
$$+ \frac{1}{4\sqrt{2\pi(\sigma_2^2+\sigma_3^2)}} \exp(\frac{-\omega^2}{2(\sigma_2^2+\sigma_3^2)}) \times \left[Q\left(\frac{-\sigma_3\omega}{\sigma_2\sqrt{\sigma_2^2+\sigma_3^2}} \right) - Q\left(\frac{-\sigma_2\omega}{\sigma_3\sqrt{\sigma_2^2+\sigma_3^2}} \right) \right] u(\omega)$$
$$+ \frac{1}{4\sqrt{2\pi}} \left[\frac{1}{\sigma_1} \exp(\frac{-\omega^2}{2\sigma_1^2}) + \frac{1}{\sigma_2} \exp(\frac{-\omega^2}{2\sigma_2^2}) + \frac{1}{\sigma_3} \exp(\frac{-\omega^2}{2\sigma_3^2}) \right] u(\omega) + \frac{1}{8}\delta(\omega) + \alpha \tag{20}$$

where

$$\alpha = \iint \left[\frac{1}{2\sqrt{2\pi}\sigma_1\sigma_2\sigma_3} \exp(\frac{-(\omega-l-v)^2}{2\sigma_1^2}) \exp(\frac{-(l)^2}{2\sigma_2^2}) \exp(\frac{-(v)^2}{2\sigma_3^2}) u(\omega-l-v) u(l) u(v) \right] d_l d_v \tag{21}$$

TABLE 3. ASE-DMT waveforms and their measured PWM-dimming range

Waveform output	Measured PWM range
Layer 1	12.5% to 87.5%
Layer 2	11.25% to 88.75%
Layer 3	12.5% to 87.5%
Sum Layer 1+2+3	16.25% to 83.75%

C. MEASUREMENT OF PWM DIMMING RANGE

The ratio of the mean to the peak amplitude of a signal determines the PWM dimming capacity. This is translated into the PWM dimming range for the individual layers and the summed ASE-DMT signal in Table 3.

Individual layers have almost a similar PWM dimming range, between 12% and 88%, while the summed ASE-DMT signal has a narrower range between 16.25% and 83.75%. For simplicity, the PWM dimming rage of 16% to 84% is assumed throughout the paper.

The PWM duty cycle is controlled in steps of 1/10. As a result, the resolution of brightness control is set at (84-16)/10 = 6.8% of the maximum brightness. The transmitter calculates the ratio of the ON and OFF pulses of the PWM control waveform, if the desired brightness level is in-between the PWM range. Otherwise, the transmitter implements the AM dimming method by scaling down the peak-to-peak amplitude so that it reaches its targeted dimming level.

D. THE SYNCHRONIZATION ALGORITHM

Two modifications are proposed for optical OFDM synchronization based on Van de Beek algorithm [19]. The first modification works with DCO-OFDM, and the second works with both DCO-OFDM and ASE-DMT. Both modifications are simple in principle. However, they result in a reliable synchronization and timing operation as explained in this section.

1) MODIFICATION 1

This modification is suitable for one-dimensional real-valued waveforms. After applying the algorithm given in [19], all the imaginary components are set to zeros and the cost function is simply equivalent to Cosi-inequality form, see Table 4.

For real-time processing, the matching of the beginning of each DCO-OFDM frame and its repetition in the cyclic prefix is based on the feed-forward concept. The matching of real-inputs is done using the algorithm set in Table 4. The maximum optimization of function $\mathbf{z}$ becomes simple since real-valued $\mathbf{z}$ is a quadratic function.

The simulation results are shown in Figures 22 and 23. The maximum value of the cost $\mathbf{z}$ function (max $\mathbf{z}$ = 0, or close to 0) happens if, and only if, a cyclic segment is entirely matched with its segment of the frame.

TABLE 4. Synchronization Algorithm 1

Input: Collect waveform segments as OFDM start segment ($\mathbf{x}$) and its cyclic prefix ($\mathbf{y}$)

$\mathbf{x} = \{x_0, x_1, \ldots, x_k\}$

$\mathbf{y} = \{y_0, y_1, \ldots, y_k\}$

Maximize: The cost function (matching function):

$$\mathbf{z} = 2\mathbf{xy} - (\mathbf{x}^2 + \mathbf{y}^2) = -(\mathbf{x} - \mathbf{y})^2 = -\sum(x_j - y_j)^2 \leq 0$$

Note: Max $\mathbf{z} = 0$ only if $(x_j = y_j)$ for all index $j = 0, 1, \ldots, k$.

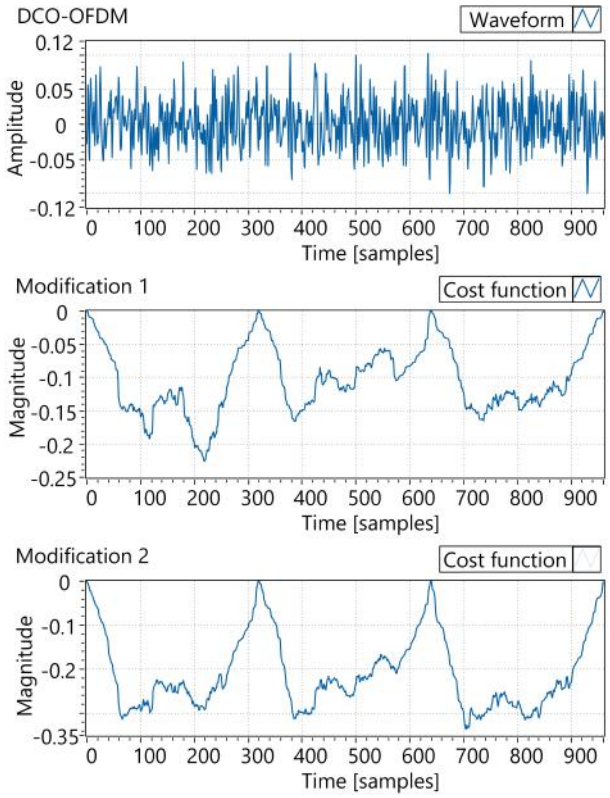

FIGURE 22. Simulation of DCO-OFDM waveform and the synchronization cost-function.

2) MODIFICATION 2

The objective of this modification is to formulate a (virtual) complex inputs for the cost function from the real-valued waveform. The optimization of the cost function now exactly the same as in [19].

Experimental results shows that modification 1 (which does not use the imaginary components) results in synchronization errors. This is due to the zero-clipping that makes the synchronization in the time domain more sensitive to noise.

Two complex inputs are derived from the received real-valued waveforms, as follows:

First step is to produce the complex inputs for ML opti-

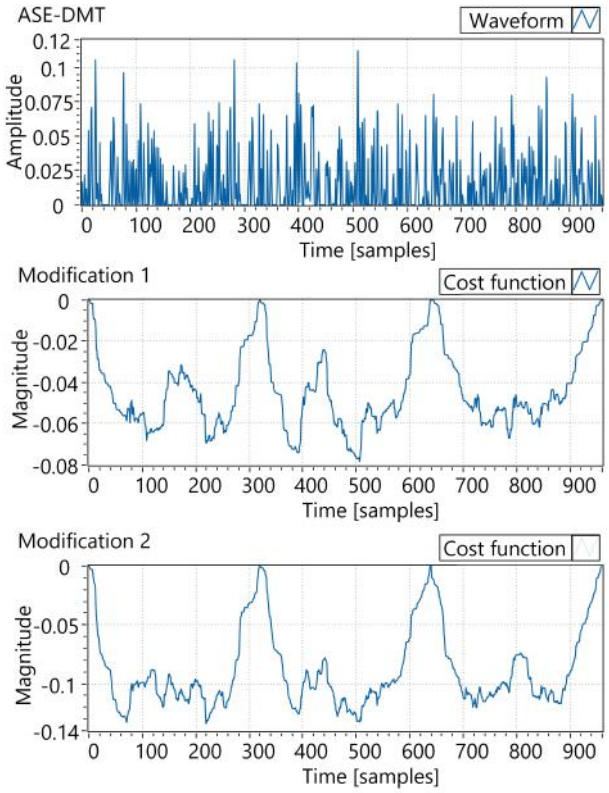

FIGURE 23. Simulation of ASE-DMT waveform and the synchronization cost-function.

mization:
• Copy the start segment of the OFDM frame index 2*m* as the real component of the input value *m*
• Copy the start segment of the OFDM frame number (2*m*+1) as the imaginary component of the input value *m*
• Copy the cyclic prefix of the OFDM frame number 2*m* as the real-component of the input value *m*+1
• Copy the cyclic prefix of the OFDM frame number (2*m*+1) as the imaginary component of the input value *m*+1

Next step is to apply ML for synchronization
• The Van de Beek ML optimization can be directly applied on complex inputs. The cost function is now defined as the log-likelihood function.
• The equality happens at the same condition of the Cauchy–Schwarz inequality (i.e. when all OFDM frames and their cyclic prefixes are matched).

Figures 22 and 23 present the simulation results for the cost functions in DCO-OFDM and ASE-DMT. Comparing the results of the two modified synchronization algorithms, Modification 2 provides more reliable and accurate timing compared to Modification 1.

Additionally, the timing accuracy in a noisy channel can be further improved if the length of the two inputs is increased.

TABLE 5. Synchronization Algorithm 2

Input: Collect waveform segments as OFDM starting segment (**x**) and its cyclic prefix (**y**)

$\mathbf{x}_{2m} = \{x_0, x_1, \ldots, x_k\}$; $\mathbf{x}_{2m+1} = \{x_N, x_{N+1}, \ldots, x_{N+k}\}$

$\mathbf{y}_{2m} = \{y_0, y_1, \ldots, y_k\}$; $\mathbf{y}_{2m+1} = \{y_N, y_{N+1}, \ldots, y_{N+k}\}$

Pre-Processing: Generate virtual complex inputs from selected segments

$\mathrm{x}_{comp}[j] = \mathrm{x}_{2m}[j] + i{*}\mathrm{x}_{2m+1}[j]$ with $j = 0, 1, \ldots, k$

$\mathrm{y}_{comp}[j] = \mathrm{y}_{2m}[j] + i{*}\mathrm{y}_{2m+1}[j]$ with $j = 0, 1, \ldots, k$

Maximize: The cost function (log-likelihood function) based on ML algorithm:

$\mathrm{Max}_{(\theta,\delta)} \Lambda(\theta, \delta) = \mathrm{Max}_{(\theta)}\ \mathrm{Max}_{(\delta)} \Lambda(\theta, \delta)$

where the log-likelihood function Λ for the arrival time θ and the carrier frequency offset δ as defined by Van de Beek et. al., [19].

In practice, the OFDM starting segments and the cyclic prefixes can be merged so that we have a longer input size for matching. By using this technique, the matching performance under low SNR becomes more robust.

VII. ANNEX 2- SOFTWARE USER INTERFACE

Figure 24 shows the experiment setup in the measurements. Figures 25-27 show a captured image of the user interface software of the ASE-DMT transmitter and receiver. In the transmitter software interface, the brightness level and PAM modulation order are both controllable. The live monitoring of constellation diagrams, the measured SNR/symbol, and demodulated data visually shows the proper operation of the system. Moreover, the receiver allows for controlling the waveform sampling and decoding. Different panels are created to separate different decoder profiles at three layers.

Figures 28 and 29 capture the transmitter and receiver software user interfaces of the DCO-OFDM system. The transmitter control panel of DCO-OFDM is very similar to ASE-DMT; however, the DCO-OFDM receiver is simpler than that of ASE-DMT because DCO-OFDM has only a single decoder.

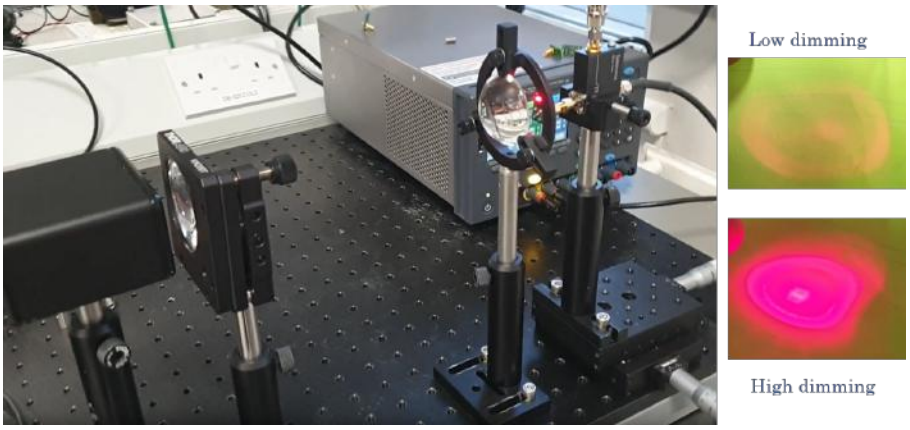

FIGURE 24. Dimming Experiment Setup.

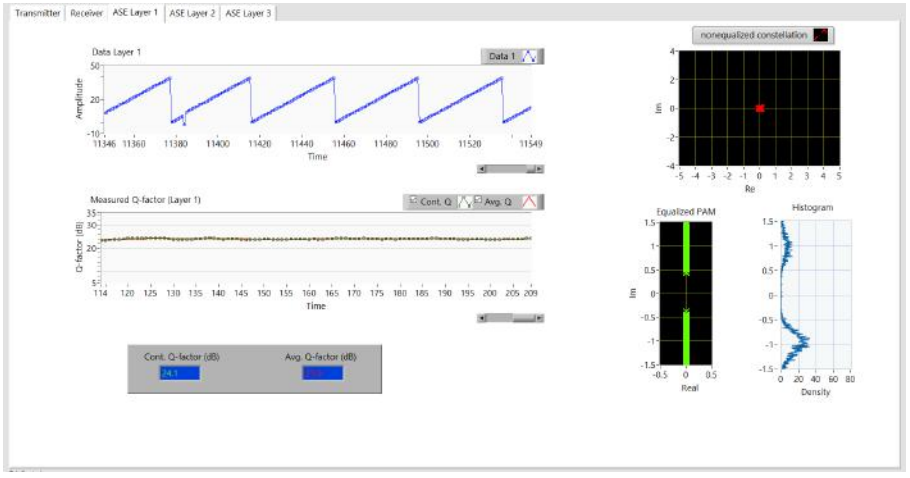

FIGURE 25. User Interface of Layer-1 Decoder of Three-layered ASE-DMT.

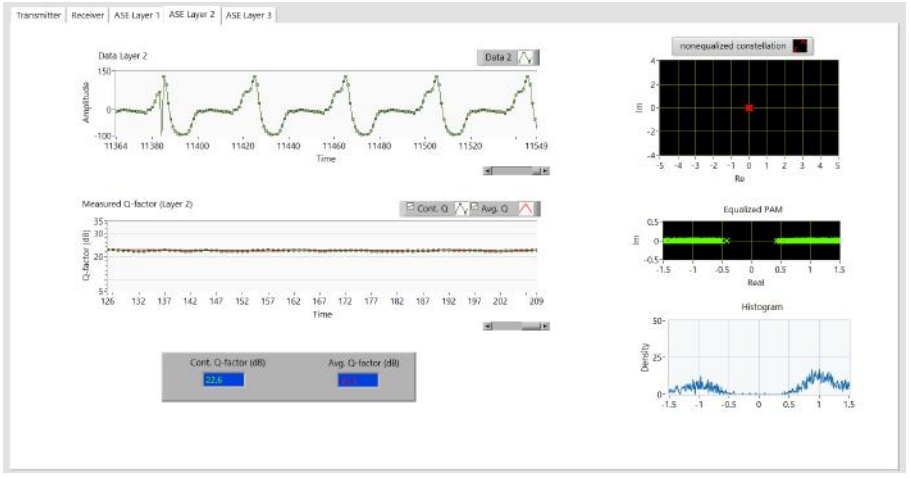

FIGURE 26. User Interface of Layer-2 Decoder of Three-layered ASE-DMT.

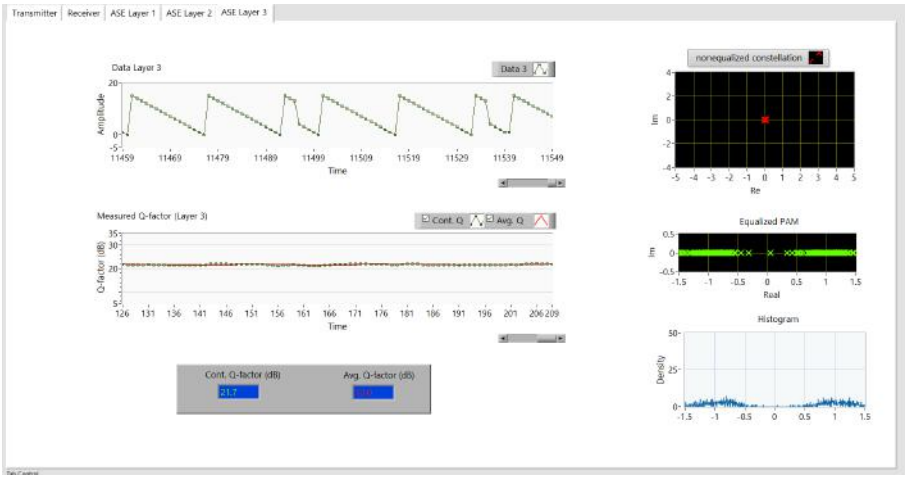

FIGURE 27. User Interface of Layer-3 Decoder of Three-layered ASE-DMT.

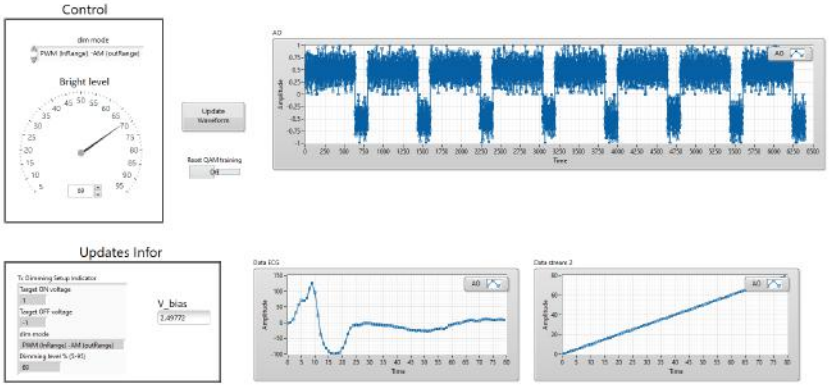

FIGURE 28. Transmitter User Interface of DCO-OFDM.

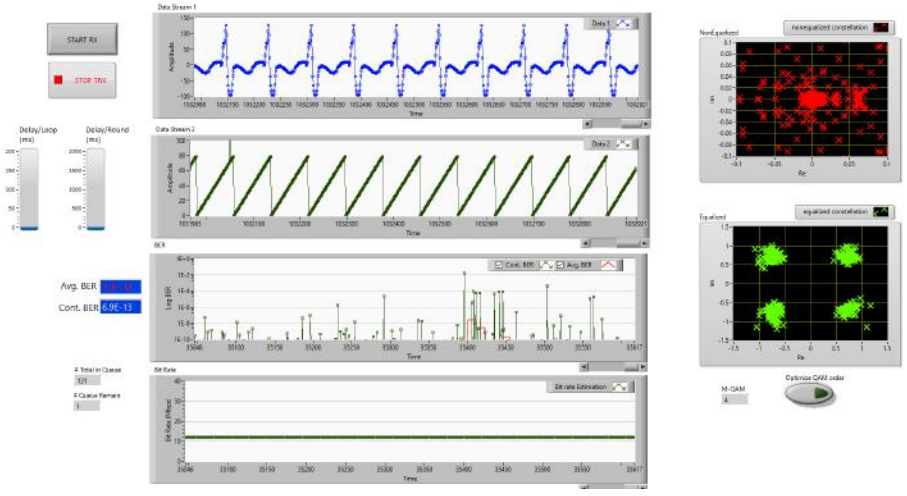

FIGURE 29. Receiver User Interface of DCO-OFDM.